A Simple Subgrid Scheme Using Space-Time Finite Integration Method

Tetsuji Matsuo, *Member, IEEE*, Tomohiro Shimoi, Jun Kawahara and, Takeshi Mifune, *Member, IEEE*

Graduate School of Engineering, Kyoto University, Kyoto 615-8510, Japan

A simple and stable subgrid scheme is derived from the space-time finite integration method, where staircase-shaped edges can be used to construct a rectangle-based grid. Comparison with classical subgrid methods shows that the proposed method suppresses unphysical wave reflection without interpolation of field values for the subgrid connection. No numerical instability was observed even after 10^6 time steps. The proposed method was applied to the computation of a photonic band gap.

Index Terms—**Finite integration method, optical-device analysis, space-time grid, subgrid.**

I. INTRODUCTION

THE ANALYSIS of metamaterial or photonic crystal often has a large computational cost because their properties are controlled by the fine structure on a sub-wavelength scale. Such analysis thus requires the generation of an adaptive grid.

The subgrid method [1]–[5] can be used to construct an adaptive Yee grid for the FDTD method. However, the subgrid method often suffers numerical instabilities and unphysical wave reflections due to nonconformal grid connections unless sophisticated techniques [1] are used. The finite integration (FI) method [5]–[7] allows the time-domain computation of electromagnetic field using unstructured spatial grids. A space-time FI method that realizes non-uniform time steps on 3D and 4D space-time grids obeying the Courant–Friedrichs–Lewy condition has been developed [8], [9]. Additionally, a local refinement of the 3D space-time grid has been realized [10], but it is not easily applied to 4D space-time because of its complex dual grid construction.

Using the space-time FI method, this study proposes a simple and stable subgrid method that realizes local refinement of the 4D space-time grid.

II. SPACE-TIME FINITE INTEGRATION METHOD

The coordinate system is denoted $(ct, x, y, z) = (x^0, x^1, x^2, x^3)$, where $c = 1 / \sqrt{(\varepsilon_0\mu_0)}$ and ε_0 and μ_0 are respectively the permittivity and permeability of a vacuum. The integral forms of the Maxwell equations [8] without source terms are

$$\oint_{\partial\Omega_p} F = 0 , \quad \oint_{\partial\Omega_d} G = 0 , \qquad (1)$$

$$F = -\sum_{i=1}^{3} E_i \mathrm{d}x^0 \mathrm{d}x^i + \sum_{j=1}^{3} cB_j \mathrm{d}x^k \mathrm{d}x^l ,$$

$$G = \sum_{i=1}^{3} H_i \mathrm{d}x^0 \mathrm{d}x^i + \sum_{j=1}^{3} cD_j \mathrm{d}x^k \mathrm{d}x^l , \qquad (2)$$

where (j, k, l) is a cyclic permutation of $(1, 2, 3)$, and Ω_p and Ω_d are hypersurfaces in space-time. The electromagnetic variables are defined in the FI method as

$$f = \int_{S_p} F , \quad g = \int_{S_d} G , \qquad (3)$$

where S_p and S_d are the faces of the primal and dual grids that constitute $\partial\Omega_p$ and $\partial\Omega_d$. To express the constitutive equation simply, the Hodge dual grid [8] is introduced as
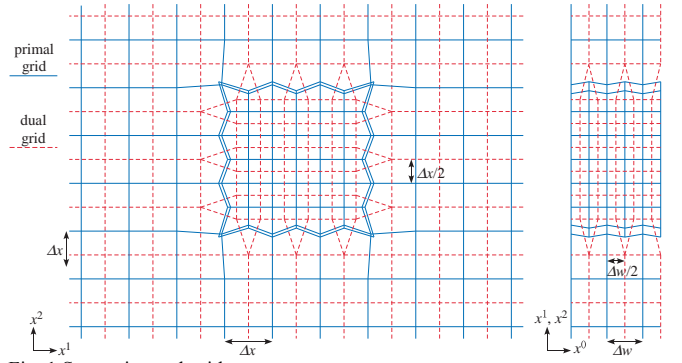
Corresponding author: T. Matsuo (e-mail: tmatsuo@kuee.kyoto-u.ac.jp).

Fig. 1 Space-time subgrid.

$$\frac{\int_{S_d} c_r \mathrm{d}x^0 \mathrm{d}x^j}{\int_{S_p} \mathrm{d}x^k \mathrm{d}x^l} = -\frac{\int_{S_d} \mathrm{d}x^k \mathrm{d}x^l}{\int_{S_p} c_r \mathrm{d}x^0 \mathrm{d}x^j} = a , \qquad (4)$$

where $c_r = 1 / \sqrt{(\varepsilon_r\mu_r)}$; a is a constant determined for each pair of S_p and S_d; and ε_r and μ_r are respectively the relative permittivity and permeability. From (3) and (4), it follows that $f = Zg / a$, where $Z = \sqrt{(\mu_r\mu_0/\varepsilon_r\varepsilon_0)}$ is the impedance.

III. 3D SPACE-TIME SUBGRID

A. Space-time grid and time-marching scheme

This study examines the subgrid shown in Fig. 1, where the primal grid (solid lines) is orthogonal to its dual grid (dashed lines) according to the Lorentzian metric [8], [9] obtained from (4). The spatial cell size and the temporal step of the coarse grid (main grid) are Δx and $\Delta w = c\Delta t$, respectively, whereas those of the fine grid (subgrid) are $\Delta x/2$ and $\Delta w/2$.

This section examines the propagation of (E_x, E_y, B_z) on the (x^0, x^1, x^2) 3D space-time grid.

The variables are allocated to primal faces and dual edges as in Fig. 2 in the domain connecting the coarse and fine grids. According to the integration (3), b and d are the magnetic and electric fluxes multiplied by c, and e and h are the temporally integrated electromotive and magnetomotive forces. Variables e and d assigned to the edges slanted with respect to the x^0-direction contain components of magnetic flux and magnetomotive force. The subscripts are spatial indexes for the x and y directions, and the superscripts are the temporal indexes. The time-marching scheme is given as

$$b_{0,0}^{1/2} = b_{0,0}^{-1/2} - e_{x,0,-1/2}^0 + e_{x,0,1/2}^0 + e_{y,-1/2,0}^0$$
$$- e_{y,1/2,-1/4}^{-1/4} - e_{y,1/2,1/4}^{-1/4} - e_{y,1/2,-1/4}^{1/4} - e_{y,1/2,1/4}^{1/4} \qquad (5)$$

$$b_{3/4,\pm1/4}^{1/4\pm1/4} = b_{3/4,\pm1/4}^{-1/4\pm1/4} - e_{x,3/4,-1/4\pm1/4}^{\pm1/4} + e_{x,3/4,1/4\pm1/4}^{\pm1/4}, \qquad (6)$$
$$+ e_{y,1/2,\pm1/4}^{\pm1/4} - e_{y,1,\pm1/4}^{\pm1/4}$$

$$h_{0,0}^{\pm1/2} = \Delta w b_{0,0}^{\pm1/2} / S_{\mathrm{BC}}, \qquad (7)$$

$$h_{3/4,\pm1/4}^{\pm1/2} = \frac{\Delta w}{2}\frac{b_{3/4,\pm1/4}^{\pm1/2}}{S_{\mathrm{BF1}}}, \quad h_{3/4,\pm1/4}^{0} = \frac{\Delta w}{2}\frac{b_{3/4,\pm1/4}^{0}}{S_{\mathrm{BF2}}}, \qquad (8)$$

$$d_{y,1/2,\pm1/4}^{-1/4} = d_{y,1/2,\pm1/4}^{-3/4} - h_{3/4,\pm1/4}^{-1/2} + h_{0,0}^{-1/2},$$
$$d_{y,1/2,\pm1/4}^{1/4} = d_{y,1/2,\pm1/4}^{-1/4} - h_{3/4,\pm1/4}^{0}, \qquad (9)$$

$$e_{y,1/2,\pm1/4}^{\pm1/4} = (\Delta w \Delta x / 4) d_{y,1/2,\pm1/4}^{\pm1/4} / (3\Delta x / 4), \qquad (10)$$

$$e_{x,0,\pm1/2}^{0} = S_{\mathrm{EC}} d_{x,0,\pm1/2}^{0} / \Delta x, \qquad (11)$$

$$e_{x,3/4,\pm1/2}^{\pm1/4} = S_{\mathrm{EF1}}\frac{d_{x,3/4,\pm1/2}^{\pm1/4}}{\Delta x / 2}, \quad e_{x,3/4,0}^{\pm1/4} = S_{\mathrm{EF2}}\frac{d_{x,3/4,0}^{\pm1/4}}{\Delta x / 2}. \qquad (12)$$

Face areas in (7), (8), (11) and (12) are given as

$$S_{\mathrm{BC}} = (\Delta x)^2 (\frac{13}{12} - \delta), \; S_{\mathrm{BF1}} = \frac{\Delta x}{2}(\frac{5}{12} + \delta)\Delta x,$$

$$S_{\mathrm{BF2}} = \frac{\Delta x}{2}[(\frac{5}{12} + \delta)\Delta x + \frac{(c_r\Delta w)^2}{6\Delta x}], \qquad (13)$$

$$S_{\mathrm{EC}} = \Delta w[(1-\delta)\Delta x - (c_r\Delta w)^2 / (12\Delta x)],$$

$$S_{\mathrm{EF1}} = \frac{\Delta w}{2}[(\frac{1}{2} + \delta)\Delta x + \frac{(c_r\Delta w)^2}{12\Delta x}],$$

$$S_{\mathrm{EF2}} = \frac{\Delta w}{2}[(\frac{1}{3} + \delta)\Delta x + \frac{(c_r\Delta w)^2}{12\Delta x}], \qquad (14)$$

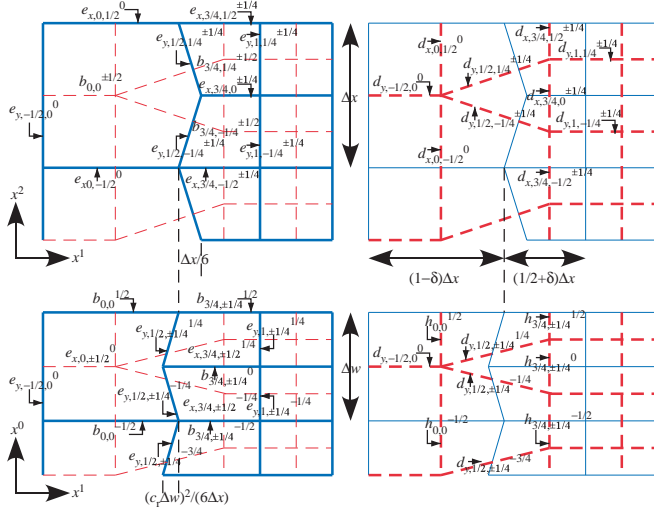where δ is a free parameter shown in Fig. 2.
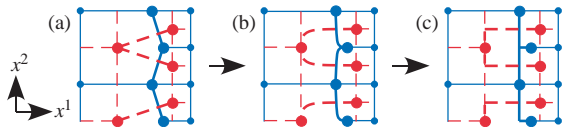

Fig. 2 Assignment of variables.

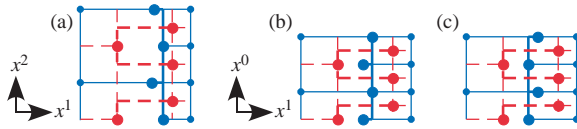Fig. 3 Transformation of edges without changing node positions (•).

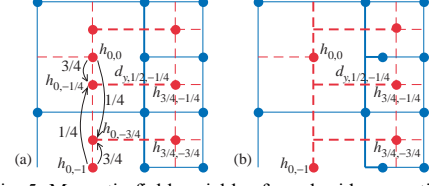Fig. 4 Alternative transformations of edges.

Fig. 5. Magnetic-field variables for subgrid connection: (a) the subgrid in [5] and (b) the proposed subgrid.

The definition of variables in the integral form (3) allows the slanted edges as in Fig. 3(a) to be curved as in Fig. 3(b), where node positions (•) are unchanged. A further transformation leads to staircase-like edges as in Fig. 3(c), where rectangular faces provide a simple FI scheme. The edge transformation is not unique. For example, staircase-like edges shown in Fig. 4(a) are also possible. The edges can be transformed along the temporal direction also, as shown Fig. 4(b) and (c). This section examines the subgrid obtained by combining the types of subgrid shown in Figs. 3(c) and 4(c). Accordingly, the face areas given as (13), (14) are replaced by

$$S_{\mathrm{BC}} = (\Delta x)^2 (1 - \delta), \; S_{\mathrm{BF1}} = (\Delta x / 2)(1/2 + \delta)\Delta x,$$

$$S_{\mathrm{BF2}} = \frac{\Delta x}{2}[(\frac{1}{2} + \delta)\Delta x + \frac{(c_r\Delta w)^2}{6\Delta x}], \qquad (15)$$

$$S_{\mathrm{EC}} = \Delta w[(1-\delta)\Delta x - (c_r\Delta w)^2 / (6\Delta x)],$$

$$S_{\mathrm{EF1}} = \frac{\Delta w}{2}[(\frac{1}{2} + \delta)\Delta x + \frac{(c_r\Delta w)^2}{6\Delta x}],$$

$$S_{\mathrm{EF2}} = \frac{\Delta w}{2}[(\frac{1}{3} + \delta)\Delta x + \frac{(c_r\Delta w)^2}{6\Delta x}], \qquad (16)$$

The subgrid scheme above requires no interpolation of field values, which results in a diagonal impedance matrix that allows stable computation. For example, as illustrated in Fig. 5(a), the subgrid method in Ref. [5] requires an interpolation such as $h_{0,-1/4} = (3h_{0,0} + h_{0,-1}) / 4$ to update $d_{y,1/2,-1/4}$. In contrast, the proposed subgrid uses $h_{0,0}$ directly to update $d_{y,1/2,-1/4}$ as in Fig. 5(b), where the staircase-like edges prevent a reduction in the computational accuracy. No interpolation or extrapolation is required along the temporal direction either, when employing the space-time FI method.

B. Numerical Examination

The growth rate of the numerical error during the temporal period Δw (= $c\Delta t$) is evaluated by numerical eigenvalue analysis [11]. A small space-time grid having a spatial domain size of $30\Delta x \times 30\Delta x$ including a subgrid domain of $14\Delta x \times 14\Delta x$ is used for the stability analysis while imposing spatially periodic boundary conditions with δ = 0. When $c_r\Delta w /\Delta x \leq$ 0.5, all the eigenvalues are on the unit circle, which implies that the time-marching scheme is numerically stable. When $c_r\Delta w /\Delta x$ exceeds 0.51, some of the eigenvalues move outside the unit circle, causing numerical instability.

Wave propagation is simulated to compare subgrid schemes on the computational domain shown in Fig. 6(a) with δ = 0. For simplicity, the permittivity and permeability are set uniformly to unity by normalization; Δx and Δw are set to 1 and 0.5 by normalization. The normalized initial conditions are $E_x = E_y = 0$ and $B_z = \exp[-(x^2 + y^2)/25]$. Spatially periodic boundary conditions are imposed. Fig. 6(b) depicts the

distribution of B_z at $ct = 60$.

Fig. 7(a) depicts the distributions of discrepancy ΔB between B_z obtained employing the FDTD method and that obtained using the proposed subgrid method at $ct = 60$. The FDTD method is executed with $\Delta x = 1$ and $\Delta w = 0.5$. The discrepancy seen for $x \geq 16$ and $y \geq 20$ is mainly caused by numerical dispersion whereas that for $x \leq 16$ or $y \leq 20$ is caused by an unphysical wave reflection at the connection with the subgrid. Fig. 7(b) and (c) depicts the distribution of ΔB obtained employing two classical subgrid techniques [3], [5]. The subgrid scheme proposed in [3] gives numerical error similar to that in Fig. 7(a). However, this scheme suffers numerical instability over long-time simulations. The subgrid scheme proposed in [5] is quite stable numerically, but yields larger numerical errors (Fig. 7(c)) than the space-time FI method. Fig. 8 compares the maximum of $|\Delta B| / |B_{max}|$ for $x \leq 16$ and $y \leq 20$ at $ct = 60$ among the three subgrid schemes when $\Delta x = 0.25, 0.5, 1, 2, 4$; the maximum magnetic flux $|B_{max}|$ is 0.09 T at $ct = 60$. The unphysical wave reflection is roughly proportional to $(\Delta x)^2$, with the use of the proposed subgrid achieving the smallest error.
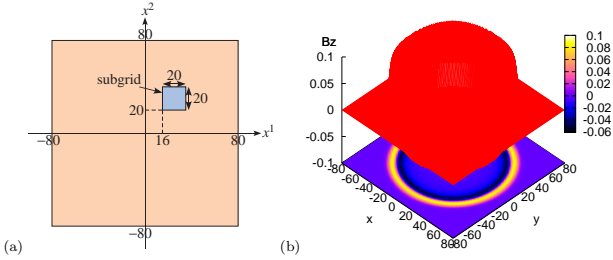

(a)　　　　　　　(b)

Fig. 6. Wave propagation computation; (a) computational domain and (b) distribution of B_z at $x^0 = 60$.
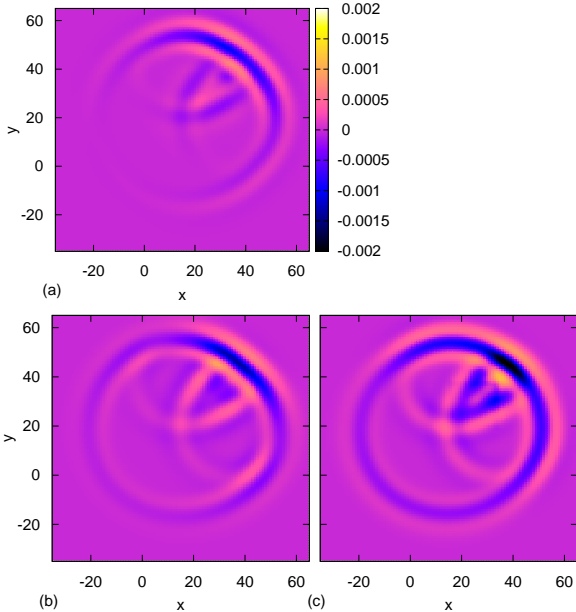

(a)

(b)　　　　　　　(c)

Fig. 7. Discrepancy in B_z relative to B_z obtained employing the FDTD method: (a) proposed subgrid, (b) subgrid in Ref. [3], and (c) subgrid in Ref. [5].

C. Application to Photonic Band Computation

Fig. 9(a) illustrates one spatial period of a 2D photonic crystal. The spatial coordinates are normalized so that one

spatial period is $[-1, 1] \times [-1, 1]$. A cylindrical rod with normalized radius of 0.4 and $\varepsilon_r = 10$ is located in the subgrid. The modulated Gaussian pulse source is located in the main grid to provide a wide-band excitation. Assuming a fixed wave number vector in the first Brillouin zone, a spatial periodic boundary condition is imposed to find the corresponding normalized angular frequencies and obtain the dispersion relation [2]. Several field probes are located randomly to obtain frequency spectra corresponding to the wave number vector. Variables (H_x, H_y, D_z) are assigned to the primal grid and (B_x, B_y, E_z) are assigned to the dual grid for the analysis of transverse-magnetic (TM) modes.

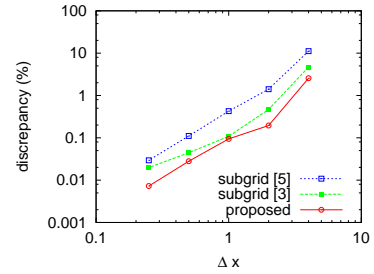

Fig. 8. Maximum of discrepancy $|\Delta B| / |B_{max}|$ relative to values obtained with the FDTD method for $x^1 \leq 16$ and $x^2 \leq 20$ with respect to grid size.
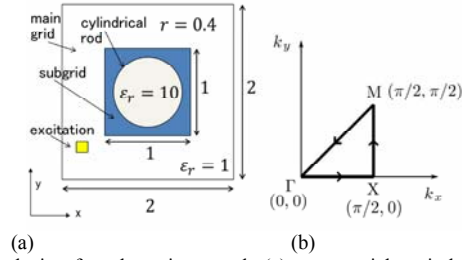

(a)　　　　　　　(b)

Fig. 9 Analysis of a photonic crystal: (a) one spatial period and (b) first Brillouin zone of the wave-number vector space.
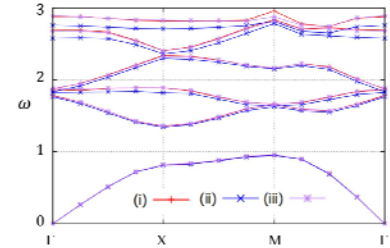

Fig. 10 Dispersion diagram for the cylindrical rod as in Fig. 9: (i) FDTD method with $\Delta x = 1/30$, (ii) FDTD method with $\Delta x = 4/30$, and (iii) space-time subgrid method with $(\Delta x, \Delta x/2) = (4/30, 2/30)$.

Fig. 10 shows a dispersion diagram of the first several TM modes obtained using (i) the FDTD method with $\Delta x = 1/30$, (ii) the FDTD with $\Delta x = 4/30$, and (iii) the proposed subgrid with $(\Delta x, \Delta x/2) = (4/30, 2/30)$. A photonic bandgap is observed between $\omega = 0.95$ and 1.38. The FI method (iii) provides a more accurate diagram than the FDTD method (ii) because of the local fine grid around the dielectric.

IV. INTRODUCTION OF A 4D SPACE-TIME SUBGRID

It is not difficult to extend the proposed simple space-time subgrid to 4D space-time. Fig. 11(a) illustrates a 4D

connection to the subgrid, where δ is a free parameter. Similarly to the case for the 3D subgrid, the edges and faces can be bent as in Fig. 11(b) and (c).

Wave propagation is simulated on the space-time grid shown in Fig. 12 under a periodic spatial boundary condition, where $\Delta x = 1$, $\Delta w = 0.4$ and $c = 1$ by normalization. The normalized initial conditions are given as $E_1 = E_2 = E_3 = 0$, $B_1 = \exp\{-[(x^2)^2+(x^3)^2]/25\}$, $B_2 = \exp\{-[(x^3)^2+(x^1)^2]/25\}$, and $B_3 = \exp\{-[(x^1)^2+(x^2)^2]/25\}$. The 4D space-time subgrid does not develop numerical instability even after $10^6\Delta w$ when $\Delta w \leq 0.4$ and $\delta \geq 0$. Fig. 13(a) depicts the discrepancy of $|B|$ from that given by the FDTD method at $x^0 = 60$, where $\delta = 0.07$. For comparison, Fig. 13(b) depicts the distribution of discrepancy $|\Delta B|$ obtained using the subgrid technique in [5], where there is larger unphysical wave reflection than in Fig. 13(a). Fig. 14 presents the maximum of $|\Delta B| / |B_{max}|$ for $x^1 \leq 16$, $x^2 \leq 20$ and $x^3 \leq 24$ at $x^0 = 60$ in the comparison of the results for the subgrid in [5] and the proposed method with $\delta = 0$, 0.07 and $|B_{max}| = 0.15$ T, when $\Delta x = 1$, 4/3, 2. The proposed subgrid with $\delta = 0.07$ provides small unphysical wave reflection.
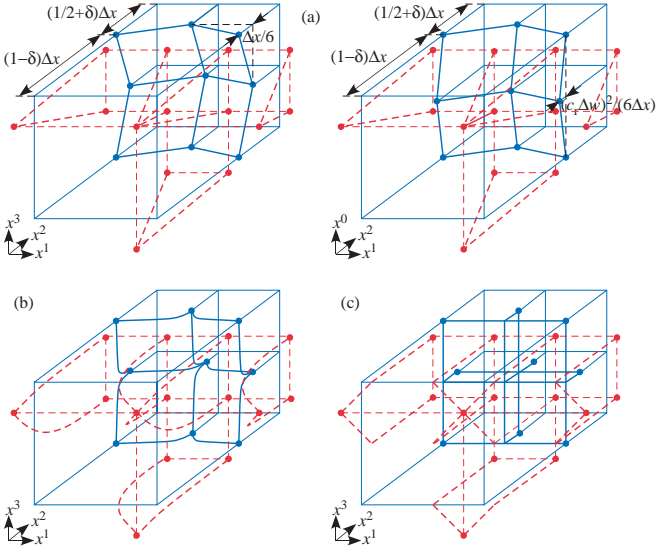

Fig. 11 4D space-time connection to a subgrid: (a) connection, (b) curved edges and faces, and (c) staircase-like edges and faces .
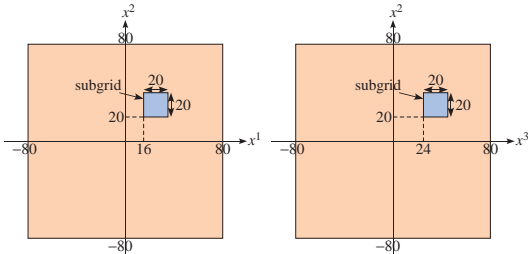

Fig. 12 3D spatial grid for the 4D space-time subgrid method.

V. CONCLUDING REMARKS

Using the space-time FI method with staircase-shaped edges, a simple and stable subgrid scheme was developed without interpolation of field values. A detailed study of the 4D subgrid connection and symmetric correction proposed in [11] will be conducted in future work to improve the accuracy of the proposed method.

REFERENCES

[1] A. Talfove and S. C. Hagness, *Computational Electromagnetics, The Finite Difference in Time Domain Method*, 3rd Ed. Chapter 11, Boston, MA: Artech House, 2005.
[2] Y. Hao and R. Mittra, *FDTD Modeling of Metamaterials: Theory and Applications.* Boston, Chapter 2, MA: Artech House, 2008.
[3] S. S. Zivanovic, K. S. Yee, and K. K. Mei, "A subgridding method for the time-domain finite-difference method to solve Maxwell's equations," *IEEE Microwave Theory Tech.*, vol. 39, pp. 471-479, 1991.
[4] K.M. Krishnaiah and C.J. Railton, "A stable subgridding algorithm and its application to eigenvalue problems," *IEEE Trans. Microwave Theory Tech.*, vol. 47, pp. 620-628, May 1999.
[5] P. Thoma and T. Weiland, "A consistent subgridding scheme for the finite difference time domain method," *Int. J. Numer. Model.*, vol. 9, pp. 359–374, 1996.
[6] R. Schuhmann and T. Weiland, "FDTD on nonorthogonal grids with triangular fillings," *IEEE Trans. Magn.*, vol. 35, pp. 1470–1473, May 1999.
[7] I. E. Lager, E. Tonti, A.T. de Hoop, G. Mur, and M. Marrone, "Finite formulation and domain-integrated field relations in electromagnetics— a synthesis," *IEEE Trans. Magn.*, vol. 39, pp. 1199–1202, May 2003.
[8] T. Matsuo, "Space-time finite integration method for electromagnetic field computation," *IEEE Trans. Magn.*, vol. 47, pp. 1530–1533, 2011.
[9] J. Kawahara, T. Mifune, and T. Matsuo, "Geometrical formulation of a 3D space-time finite integration method," *IEEE Trans. Magn.*, vol. 49, pp. 1693–1696, May 2013.
[10] T. Shimoi, T. Mifune, and T. Matsuo, "Space-time finite integration method using local fine grid for electromagnetic wave computation," in *2013 IEEE APSURSI,* Orlando, FL, pp. 1652–1653, 2013.
[11] T. Matsuo and T. Mifune, "Reduction of unphysical wave reflection arising from space-time finite integration method," *IEEE Trans. Magn,*. vol. 50, 7004204, February 2014.
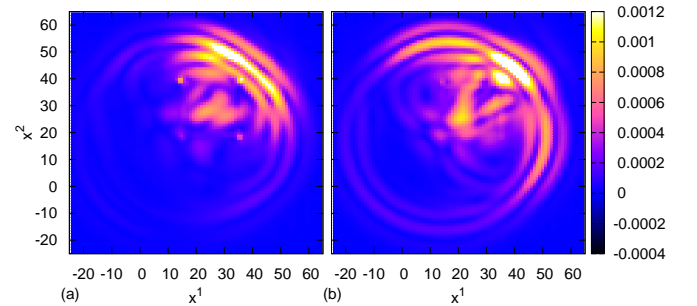
Fig. 13 Discrepancy in $|B|$ at $x^3 = 34$ relative to values obtained with the FDTD method: (a) proposed subgrid and (b) subgrid in Ref. [5].

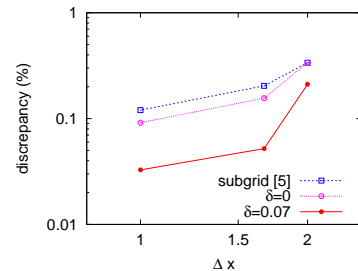Fig. 14 Maximum of discrepancy $|\Delta B| / |B_{max}|$ relative to values obtained with the FDTD method for $x^1 \leq 16$, $x^2 \leq 20$ and $x^3 \leq 24$ with respect to grid size.